

Delineation of thermodynamic and dynamic responses to sea surface temperature forcing associated with El Niño

Xiaoming Hu^{1,2} · Ming Cai³ · Song Yang^{1,2,4} · Zhaohua Wu^{3,5}

Received: 19 November 2016 / Accepted: 26 April 2017 / Published online: 3 May 2017
© The Author(s) 2017. This article is an open access publication

Abstract A new framework is proposed to gain a better understanding of the response of the atmosphere over the tropical Pacific to the radiative heating anomaly associated with the sea surface temperature (SST) anomaly in canonical El Niño winters. The new framework is based on the equilibrium balance between thermal radiative cooling anomalies associated with air temperature response to SST anomalies and other thermodynamic and dynamic processes. The air temperature anomalies in the lower troposphere are mainly in response to radiative heating anomalies associated with SST, atmospheric water vapor, and cloud anomalies that all exhibit similar spatial patterns. As

a result, air temperature induced thermal radiative cooling anomalies would balance out most of the radiative heating anomalies in the lower troposphere. The remaining part of the radiative heating anomalies is then taken away by an enhancement (a reduction) of upward energy transport in the central-eastern (western) Pacific basin, a secondary contribution to the air temperature anomalies in the lower troposphere. Above the middle troposphere, radiative effect due to water vapor feedback is weak. Thermal radiative cooling anomalies are mainly in balance with the sum of latent heating anomalies, vertical and horizontal energy transport anomalies associated with atmospheric dynamic response and the radiative heating anomalies due to changes in cloud. The pattern of Gill-type response is attributed mainly to the non-radiative heating anomalies associated with convective and large-scale energy transport. The radiative heating anomalies associated with the anomalies of high clouds also contribute positively to the Gill-type response. This sheds some light on why the Gill-type atmospheric response can be easily identifiable in the upper atmosphere.

This paper is a contribution to the special issue on East Asian Climate under Global Warming: Understanding and Projection, consisting of papers from the East Asian Climate (EAC) community and the 13th EAC International Workshop in Beijing, China on 24–25 March 2016, and coordinated by Jianping Li, Huang-Hsiung Hsu, Wei-Chyung Wang, Kyung-Ja Ha, Tim Li, and Akio Kitoh.

✉ Ming Cai
mcai@fsu.edu

✉ Song Yang
yangsong3@mail.sysu.edu.cn

¹ School of Atmospheric Sciences, Sun Yat-sen University, 135 West Xingang Road, Guangzhou 510275, China

² Guangdong Province Key Laboratory for Climate Change and Natural Disaster Studies, Sun Yat-sen University, Guangzhou, China

³ Department of Earth, Ocean and Atmospheric Sciences, Florida State University, Tallahassee, FL, USA

⁴ Institute of Earth Climate and Environment System, Sun Yat-sen University, Guangzhou, China

⁵ Center for Ocean-Atmospheric Prediction Studies, Florida State University, Tallahassee, USA

Keywords El Niño · SST anomalies · Thermodynamic and dynamic responses · Gill-type response

1 Introduction

The hallmark of an El Niño, in terms of sea surface temperature (SST) anomalies, is the pattern of anomalous warming in the equatorial central-eastern Pacific and cooling in the western equatorial Pacific (Bjerknes 1969; Larkin 2005; Kao and Yu 2009). Associated with the anomalous SST pattern is an eastward shift of the rising branch of the Walker Circulation from the equatorial western

Pacific to the central Pacific. The eastward shifting of the Walker Circulation is manifested by upward (downward) motion anomalies and anomalous divergence (convergence) in the upper troposphere over the central equatorial (western) Pacific region (Zebiak 1986; Trenberth et al. 1998; Ashok et al. 2007; Yuan and Yang 2012). Associated with the anomalous divergence flow is a pair of off-equator anti-cyclonic circulation anomalies on the west and an equatorial positive center of geopotential height anomaly on the east (Gill 1980; Rasmusson and Kingtse 1993). For an easy reference, we refer to such spatial pattern of geopotential height anomaly as a positive “tripod” of circulation anomalies. The off-equator anti-cyclonic circulation anomalies serve as the source of Rossby wave train emanating from deep tropic into the extratropics along the great circle route (Hoskins and Karoly 1981; Philander 1990; Trenberth et al. 1998). In this way, an El Niño leads to profound impacts on weather and climate over the globe, including remote regions via teleconnections (Wang et al. 2000, 2012; Alexander et al. 2002; Lyon and Barnston 2005; Ashok et al. 2007). Besides this positive tripod, there exists a negative tripod associated with the downward motion anomalies over the western equatorial Pacific, namely a pair of off-equator anomalous cyclonic centers on the west and a negative geopotential height center on the east centered at around 150°E (DeWeaver and Nigam 2004).

Gill (1980) provided an analytic solution of the idealized atmospheric dynamic response to a localized diabatic heating anomaly center, which exhibits a positive tripod spatial pattern. It represents the dynamic balance of a pair of westward propagating Rossby anti-cyclonic circulation anomalies and an eastward propagating high-pressure Kelvin mode in the upper troposphere with the positive diabatic heating anomalies below. Conversely, a negative tripod spatial pattern in the upper troposphere can be regarded as the Gill-type response to a diabatic cooling anomaly. DeWeaver and Nigam (2004) used a linear general circulation model to prove that in the upper troposphere during the mature phase of El Niño events, the co-existence of a positive tripod of circulation anomalies over the central tropical Pacific and a negative tripod above the western tropical Pacific can be regarded as the Gill-type response to a pair of localized heating anomalies of opposite sign with positive value in the east and negative value in the west (see Fig. 1a).

The Gill solution also predicts that there is a tripod with the opposite sign in the lower troposphere centered at the localized diabatic heating center (Wu et al. 2000; Wu 2003). In other words, one would expect a negative (positive) tripod spatial pattern over the central/eastern (western) tropical Pacific in the lower troposphere during

El Niño events, if the Gill-type response would prevail. During El Niño events, the surface pressure anomalies and geopotential height anomalies in the lower troposphere exhibit negative values over the tropical eastern Pacific but positive values over the western equatorial Pacific, indicating a negative Southern Oscillation pattern (Rasmusson and Carpenter 1982; Rasmusson and Wallace 1983). However, the accompanied off-equator circulation anomalies of the same sign as in the Gill-type response are unpronounced or too far away (about 5°–10° of latitude further away from the equator) from the equator in the lower troposphere (Fig. 1f or 2c). The lack of Gill-type dynamic response signal in the lower atmosphere seems to indicate that the thermodynamic response would have to play a more important role in the observed response to SST anomalies in the lower troposphere. Thermodynamic processes yield different spatial patterns in the lower-tropospheric response to SST anomalies of El Niño events, especially near the surface (Lindzen and Nigam 1987; Battisti et al. 1999; Chiang et al. 2001; Back and Bretherton 2009). Battisti et al. (1999) found that the circulation anomalies near the surface were forced by sensible and latent heat flux anomalies while circulation anomalies above the boundary layer were forced by the latent heating anomaly. Furthermore, Chiang et al. (2001) reported that the Gill type response above the boundary layer contributed significantly to the surface zonal wind but the meridional wind was primarily forced by the gradient of SST anomalies associated with El Niño events. Back and Bretherton (2009) and Zhang et al. (2012) discussed the relative contributions from the thermodynamic process in the boundary layer and the dynamic process above the boundary layer. The existence of clearly organized Gill-type response in the middle and upper troposphere but less organized one in the lower troposphere was duplicated in model simulations of El Niño (Lee et al. 2009).

The main objective of this study is to delineate the roles of the thermodynamic and dynamic responses to SST anomalies associated with canonical El Niño events. Geopotential height (z') and air temperature anomalies (T') are related to one another via the hydrostatic balance (or the hypsometric equation), namely,

$$z'_{upper_level} = z'_{lower_level} + \frac{RT'}{g} \ln \frac{p_{lower_level}}{p_{upper_level}}, \quad (1)$$

where g is the gravity and T' corresponds to the air temperature anomalies in the layer between two isobaric surfaces p_{lower_level} and p_{upper_level} . Therefore, one can infer the geopotential height anomalies at an isobaric surface above 1000 hPa from geopotential height anomalies at 1000 hPa

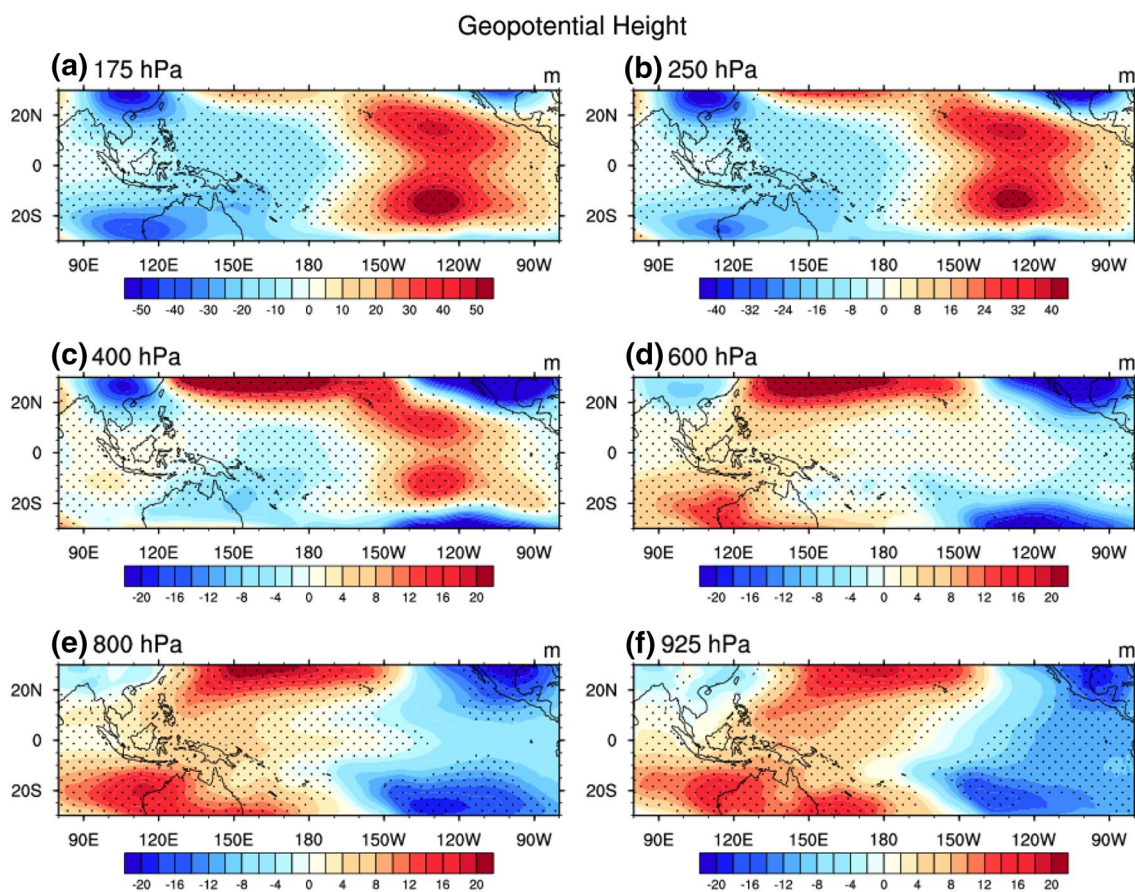


Fig. 1 Composite DJF-mean anomalies in El Niño winters of observed geopotential height anomalies in units of m at **a** 175 hPa, **b** 250 hPa, **c** 400 hPa, **d** 600 hPa, **e** 800 hPa, and **f** 925 hPa. Stippling indicates the 90% confidence level of statistical significance. Zonal means are excluded

and the temperature anomalies in the layers below the isobaric surface under consideration. In particular, as elevation increases, positive geopotential height anomalies are co-located with warm temperature anomalies and negative height anomalies with cold temperature anomalies. In this light, we will focus on air temperature response in this study. Specifically, we wish to examine how the response in atmospheric temperature transitions from the thermodynamically-driven response in the lower troposphere, which resembles to the SST anomaly pattern, to the pattern characterized by the Gill-type response in the upper atmosphere. The remaining part of this paper is organized as follows. Section 2 presents the analysis framework of the coupled dynamic and thermodynamic responses and Sect. 3 describes data and analysis procedures. The features of atmospheric response to SST anomalies associated with El Niño events are presented in Sect. 4. Section 5 discusses the attribution of temperature response to individual radiative and non-radiative heating anomalies. Conclusions are given in Sect. 6.

2 Analysis framework

A new framework is proposed to delineate the atmosphere response to SST anomalies. The main feature of this new framework is to divide loosely the atmosphere response to anomalous upward longwave radiative fluxes associated with SST anomalies into two parts: non-temperature response and temperature response. Non-temperature response includes the changes in atmospheric dynamics processes, such as those in convective activity and large-scale atmospheric circulation (e.g., the Gill-type response), as well as the changes in non-temperature thermodynamic variables such as water vapor and cloud anomalies. The changes in atmospheric dynamics processes redistribute energy both vertically and horizontally far away from the original diabatic heating anomaly, but also generate additional heating anomalies, such as latent heat anomalies. Associated with the changes in non-temperature thermodynamic variables are radiative heating anomalies. It is the anomaly of thermal radiative

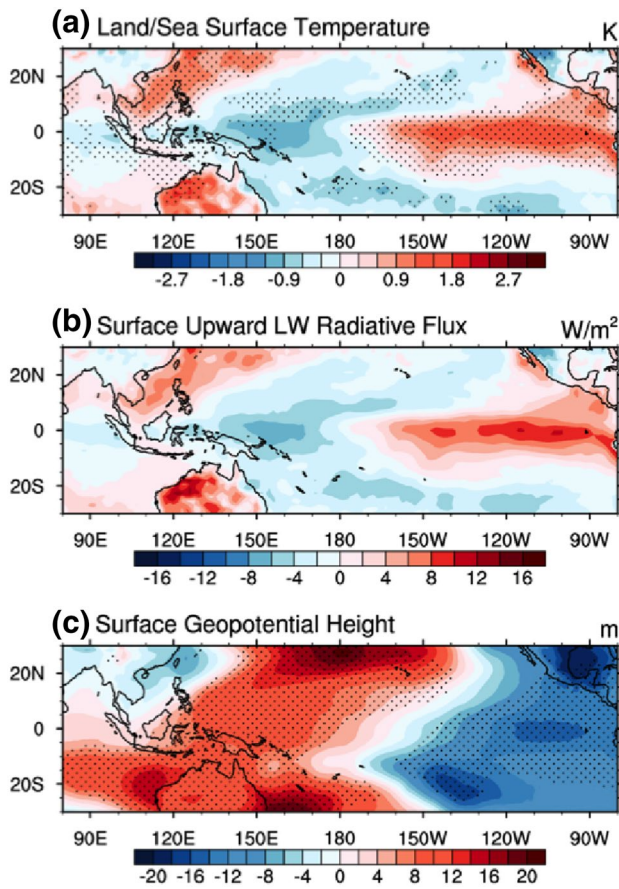


Fig. 2 Composite DJF-mean anomalies in El Niño winters of observed **a** land and sea surface temperature anomalies (K), **b** upward longwave radiative flux anomalies (W/m^2), and **c** geopotential height anomalies (m) at 1000 hPa. Stippling indicates the 90% confidence level of statistical significance. Zonal means are excluded

cooling rate associated with the changes in air temperatures that is in balance with the sum of these individual non-temperature induced radiative heating anomalies and non-radiative energy flux convergence anomalies.

The formulation of the new framework is based on the perturbation equation of energy balance in an atmospheric layer j , namely,

$$\Delta^{(RAD)}Q_j + \Delta^{(DYN)}Q_j = 0, \tag{2}$$

where $\Delta^{(RAD)}Q_j$ corresponds to the total changes in the net radiative heating rate within the layer. $\Delta^{(DYN)}Q_j$ corresponds to the non-radiative energy flux convergence anomalies into the layer, which are equal to the sum of perturbations in energy redistributions by convective and large-scale atmospheric motions as well as changes in energy fluxes entering the atmosphere due to the changes in surface sensible and latent heat fluxes. Note that in (2) we neglect the heat storage term in atmospheric layers, which is very small for

interannual-scale phenomena such as El Niño. By evoking a linear approximation, we have

$$\begin{aligned} \Delta^{(RAD)}Q_j \approx & \Delta^{(T_{below})}Q_j + \Delta^{(T_{above})}Q_j + \Delta^{(WV)}Q_j \\ & + \Delta^{(C)}Q_j - \Delta^{(T_j)}R_j + \Delta^{(other)}Q_j, \end{aligned} \tag{3}$$

where $\Delta^{(T_{below})}Q_j$ is the absorption of the perturbation longwave radiative flux of the layer emitted from the layers below associated with air/surface temperature anomalies, whereas $\Delta^{(T_{above})}Q_j$ is the absorption of the perturbation longwave radiative flux of the layer emitted from the layers above associated with air temperature anomalies there. $\Delta^{(WV)}Q_j$ and $\Delta^{(C)}Q_j$ are the net radiative heating rate perturbations of the layer due to the changes in atmospheric water vapor (WV) and clouds (C), respectively. $\Delta^{(T_j)}R_j$ is the radiative thermal cooling rate anomalies due to atmospheric temperature anomalies of the layer (T_j), and $\Delta^{(other)}Q_j$ denotes the net radiative heating rate perturbation of the layer due to the changes in stratospheric ozone and surface albedo. Because the part of $\Delta^{(other)}Q_j$ due to the change in ozone is very small in the troposphere and the part of $\Delta^{(other)}Q_j$ due to the change in surface albedo is nearly equal to zero over tropical oceans, we neglect the term $\Delta^{(other)}Q_j$ in this study. Combining (2) and (3) without the term $\Delta^{(other)}Q_j$ yields

$$\Delta^{(T_j)}R_j \approx \Delta^{(T_{below})}Q_j + \Delta^{(T_{above})}Q_j + \Delta^{(WV)}Q_j + \Delta^{(C)}Q_j + \Delta^{(DYN)}Q_j. \tag{4}$$

Next, we calculate the pattern-amplitude projection (PAP; Deng et al. 2012) coefficients according to

$$PAP_j^{(X)} = \frac{A^{-1} \int_A a^2 \Delta^{(X)}Q_j \Delta^{(T_j)}R_j \cos \phi d\lambda d\phi}{\sqrt{A^{-1} \int_A a^2 (\Delta^{(T_j)}R_j)^2 \cos \phi d\lambda d\phi}}, \tag{5}$$

where ϕ and λ are respectively latitude and longitude, and a is the radius of the earth, and the symbol “A” denotes the area of the tropical Pacific domain of 30°S – 30°N , 90°E – 90°W . $\Delta^{(X)}Q_j$ is one of the terms on the right hand side (RHS) of (3) in the j th atmospheric layer. The summation of $PAP_j^{(X)}$ over all terms on the RHS of (4) is approxi-

mately equal to the amplitude of the spatial pattern of $\Delta^{(T_j)}R_j$ over the area A ($\sum_X PAP_j^{(X)} \approx \sqrt{A^{-1} \int_A a^2 (\Delta^{(T_j)}R_j)^2 \cos \phi d\lambda d\phi}$), indicating

that the approximation in (3) is valid (the approximation is due to the linearization of the radiative transfer model and the neglecting of the small term $\Delta^{(other)}Q_j$). $PAP_j^{(X)}$ measures the relative contribution of each term on the RHS of (4) to $\Delta^{(T_j)}R_j$ in the j th atmospheric layer in terms of both spatial pattern and amplitude. It follows that the closer the

value of $PAP_j^{(X)}$ to the amplitude of the spatial pattern of $\Delta^{(T_j)}R_j$, the larger the contribution of the corresponding process to both spatial pattern and amplitude of temperature response. Thus, we can say that the atmospheric temperature change in the layer over area A is mainly in response to the process X because the radiative cooling associated with air temperature change ($\Delta^{(T_j)}R_j$) is mainly in balance with $\Delta^{(X)}Q_j$.

3 Data and analysis procedures

The data used in this study are obtained from the European Centre for Medium-range Weather Forecasts (ECMWF) Re-Analysis Interim (ERA-Interim; Dee and Uppala 2009; Dee et al. 2011). The atmospheric variables include geopotential height, air temperature, specific humidity, ozone mixing ratio, cloud cover, and cloud liquid/ice water content. All atmospheric variables are defined at 37 pressure levels from 1000 to 1 hPa. We also consider the incoming solar energy flux at the top of the atmosphere (TOA), the surface skin temperature, the upward longwave radiative flux at the surface, surface albedo, and surface sensible/latent heat fluxes.

Following Hu et al. (2016), we use the data in the periods of the four major canonical El Niño winters (1982/1983, 1986/1987, 1997/1998, and 2006/2007) and eight ENSO-neutral winters (1980/1981, 1981/1982, 1985/1986, 1989/1990, 1992/1993, 1993/1994, 2001/2002, and 2003/2004) to construct the composite El Niño and neutral events, respectively. The differences (denoted by the symbol Δ) between the composite El Niño and neutral events are referred to as El Niño anomalies. We focus on the El Niño anomalies over the tropical Pacific and part of the East Asia monsoon region (30°S–30°N, 80°E–80°W).

We use the Fu-Liou radiative transfer model (Fu and Liou 1992, 1993) to evaluate all terms in (2) at the original 37 levels of the ERA-interim on each grid point as the following:

where Q_j is the net radiative energy flux convergence (in units of W/m²) in each atmospheric layer obtained from the radiative transfer model using the information of T , WV , and C , as well as other variables/parameters (denoted as “other”) such as the incoming solar radiative flux at the TOA, ozone, and surface albedo. The superscript “N” and “E” denote, respectively, the variables derived from the composite mean fields of the eight ENSO-neutral winters and the four major El Niño winters. In (6), subscript “all” denotes temperature in all layers including the surface level. Subscripts “below_j” and “other_b” represent the temperatures in the layers below j (which includes SST) and the temperatures in the remaining layers, respectively. Subscripts “above_j” and “other_a” denote the temperatures in the layer above j and the remaining layers respectively, and “j” and “other_j” denote the temperatures at the layer j and in other layers respectively. Note that the vertical profiles of C include cloud liquid and ice water as well as cloud area. We then use (2) to infer the term $\Delta^{(DYN)}Q_j$ indirectly as

$$\Delta^{(DYN)}Q_j = -\Delta^{(RAD)}Q_j. \tag{7}$$

Equations (6) and (7) enable us to obtain all of the terms in (4). It can be verified that the approximation (3) is indeed valid, implying that the perturbation of total net radiative heating rate in each layer can be linearly decomposed into individual terms given in (6).

Note that because the units of all terms in (6) have been converted from K/s (degree per second) to W/m², they can be summed up vertically without changing their physical meanings. For example, the vertical summation of $\Delta^{(WV)}Q_j$ from the lowest to the highest atmospheric layers corresponds to the perturbation in the net radiative heating rate by the atmosphere due to the changes in atmospheric water vapor. Therefore, we can reduce the number of layers in our discussions to a few selected layers by adding the terms vertically. We have divided the atmospheric column broadly into six layers in presenting the results of (3) and (4): one for the boundary layer (1000–925 hPa), two for the lower troposphere (925–800 hPa and 800–600 hPa), one

$$\begin{aligned} \Delta^{(RAD)}Q_j &= Q_j(T_{all}^E, WV^E, C^E, other^E) - Q_j(T_{all}^N, WV^N, C^N, other^N) \\ \Delta^{(T_{below})}Q_j &= Q_j(T_{below_j}^E, T_{others_b}^N, WV^N, C^N, other^N) - Q_j(T_{all}^N, WV^N, C^N, other^N) \\ \Delta^{(T_{above})}Q_j &= Q_j(T_{above_j}^E, T_{others_a}^N, WV^N, C^N, other^N) - Q_j(T_{all}^N, WV^N, C^N, other^N) \\ \Delta^{(WV)}Q_j &= Q_j(T_{all}^N, WV^E, C^N, other^N) - Q_j(T_{all}^N, WV^N, C^N, other^N) \\ \Delta^{(C)}Q_j &= Q_j(T_{all}^N, WV^N, C^E, other^N) - Q_j(T_{all}^N, WV^N, C^N, other^N) \\ \Delta^{(T_{air})}R_j &= -\left[Q_j(T_j^E, T_{other_j}^N, WV^N, C^N, other^N) - Q_j(T_{all}^N, WV^N, C^N, other^N)\right] \\ \Delta^{(other)}Q_j &= Q_j(T_{all}^N, WV^N, C^N, other^E) - Q_j(T_{all}^N, WV^N, C^N, other^N), \end{aligned} \tag{6}$$

for the middle troposphere (600–400 hPa), and two for the upper troposphere (400–250 hPa and 250–150 hPa). We will explain geopotential height anomalies at the interface levels (i.e., 925, 800, 600, 400, 250, and 150 hPa) from sea-level pressure anomalies and the layer temperature resulted according to (1).

4 An overview of the key features of atmospheric anomalies of El Niño events

We here present an overview of the salient features of atmospheric circulation anomalies observed during El Niño events. During El Niño winters, the geopotential height anomalies over the tropical Pacific at various levels corresponded to the composite SST anomalies (Fig. 2a) are displayed in Fig. 1. It shows that in the upper troposphere above 500 hPa, there exists a pair of negative and positive tripods of circulation anomalies centered over the western and eastern tropical Pacific, respectively (Fig. 1a and b). The intensity of geopotential height anomalies is strongest at 200 hPa. The existence of such a pair of tripods in the upper troposphere is consistent with the Gill-type response to a pair of localized heating anomalies of opposite sign

with positive values in the east and cooling anomalies in the west (DeWeaver and Nigam 2004). Below the middle troposphere (Fig. 1d–f), the geopotential height response mainly shows negative values over the tropical eastern Pacific but positive values over the western Pacific, indicating the negative Southern Oscillation pattern during El Niño winters (Rasmusson and Wallace 1983; Scherllin-Pirscher et al. 2011). The off-equator positive and negative centers in the low-level are far away from the equator. Therefore, the canonical low-level Gill-type response is not observed in the lower troposphere. The lack of Gill-type dynamic response signal in the lower atmosphere seems to indicate that the thermodynamic response could play a more important role in the observed response to SST anomalies in the lower troposphere.

It is seen from Fig. 3 that the spatial pattern of air temperature anomalies in the lower troposphere is similar to SST anomalies, including the positive and negative centers that are far away from the equator. The Gill-type response begins to emerge clearly at 500 hPa with the maximum intensity at 300 hPa. Therefore, one would infer from the hydrostatic balance that the pair of tripod patterns in geopotential height anomalies exists only at levels above 500 hPa with the maximum intensity at 300 hPa. According

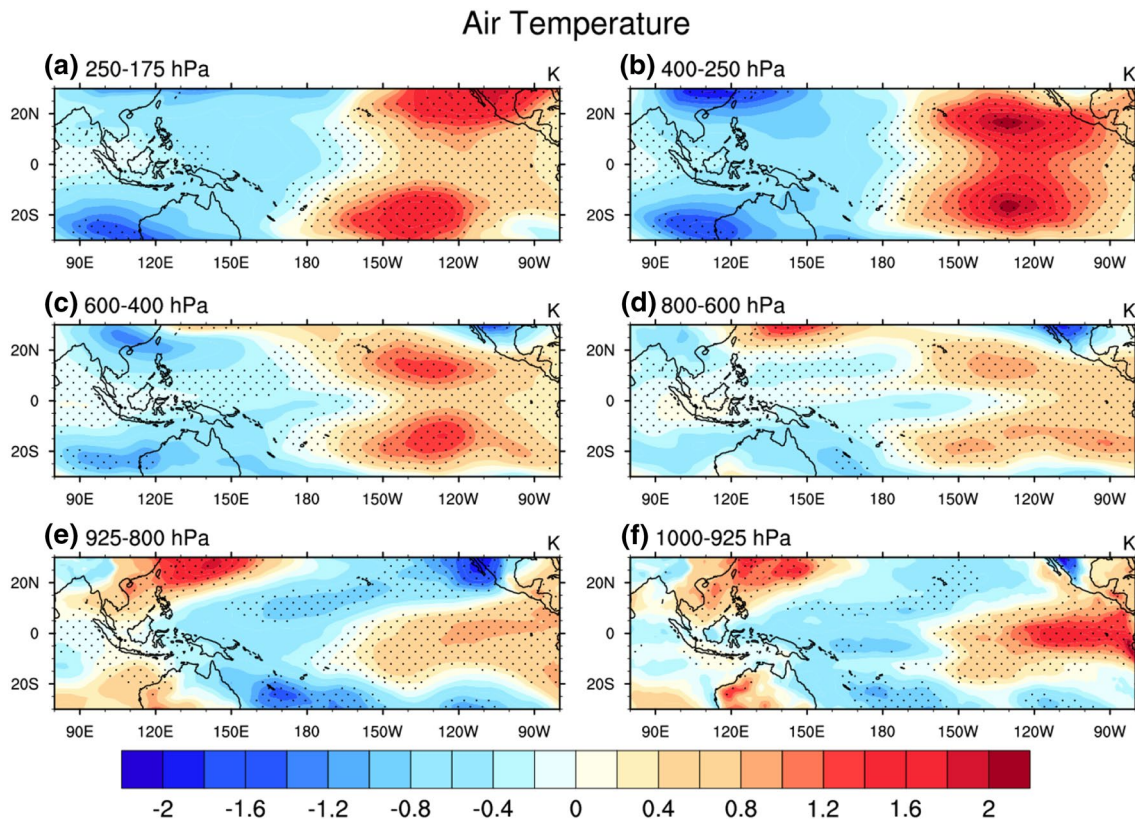


Fig. 3 As in Fig. 1 but for mass-weighted mean layer temperature anomalies (K) in the layers of **a** 250–175 hPa, **b** 400–250 hPa, **c** 600–400 hPa, **d** 800–600 hPa, **e** 925–800 hPa, and **f** 1000–925 hPa

to Fig. 1, the maximum amplitude of the tripod patterns in the field of geopotential height anomaly is at 200 hPa. The ability of using the hydrostatic balance (1) to infer geopotential height anomalies from air temperature response to SST anomalies is the rationale that prompts us to focus on air temperature response in the framework of (4) for explaining the dominance of the thermodynamically-driven response in the lower troposphere but the Gill-type response in the upper troposphere.

Now let us examine the anomaly fields that are responsible for the energy flux convergence perturbations on the RHS of (4). The anomalous upward longwave radiative flux emitted from the surface during El Niño events (ΔR_S^\uparrow , Fig. 2b) can be inferred directly from the corresponding SST anomalies (Fig. 2a) using $\Delta R_S^\uparrow \approx 4\sigma \bar{T}_S^3 \Delta T_S$, where σ is the Stefan–Boltzmann constant and \bar{T}_S is the mean SST derived from the composite mean of neutral events. The term ΔR_S^\uparrow can be regarded as the “source of external forcing” for the atmospheric response since its absorption by the atmosphere, i.e. the first term on the RHS of (4) for $j=1$ or the layer centered around 950 hPa, is a source of energy outside the atmosphere component of the coupled atmosphere–ocean system in the analysis framework (4). Here we

wish to reiterate that the anomalous surface latent and sensible fluxes are also “external forcings” to the atmosphere component. Since the ERA-Interim does not include the information about non-radiative diabatic heating rates in the atmosphere, the effect of anomalous surface latent and sensible fluxes entering the atmosphere has been blended in the last term on its RHS as the perturbation of the sum of non-radiative diabatic heating rate and convective/advective energy flux convergence.

The atmospheric water vapor anomalies of the composite El Niño (Fig. 4) exhibit a similar spatial pattern as the SST anomalies, showing a moistening center in the equatorial central and eastern Pacific but drying anomalies in the western equatorial Pacific and the off-equator tropical latitudes in both hemispheres. This feature is consistent with the results of Prabhakara et al. (1985) and Takahashi et al. (2013). The horizontal pattern of atmospheric water vapor anomalies remains largely unchanged throughout the troposphere but its amplitude decreases gradually with height in the lower troposphere and diminishes in the upper troposphere. The cloud water/ice content anomalies of the composite El Niño, however, exhibit large amplitude in the middle and upper troposphere (Fig. 5b–d). The spatial

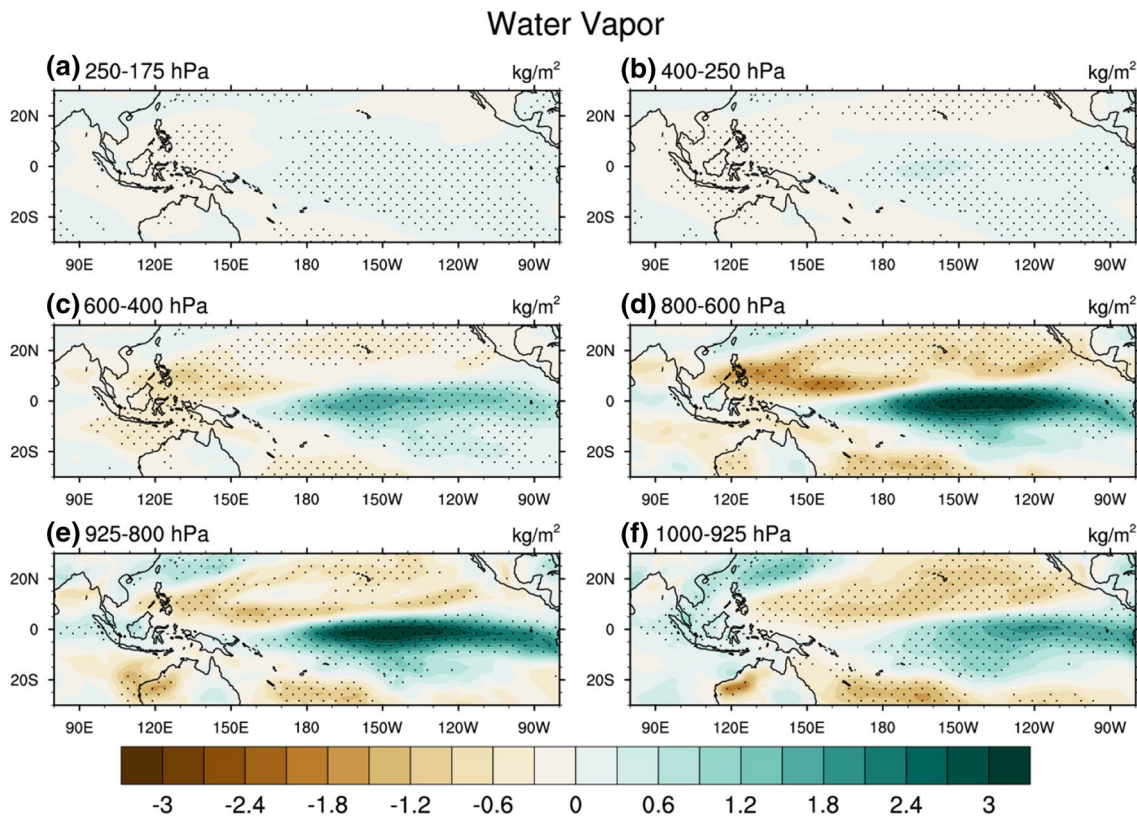


Fig. 4 Composite DJF-mean anomalies in El Niño winters of observed water vapor anomalies in units of kg/m^2 in the layer of **a** 250–150 hPa, **b** 400–250 hPa, **c** 600–400 hPa, **d** 800–600 hPa, **e** 925–

800 hPa, and **e** 1000–925 hPa. Stippling indicates the 90% confidence level of statistical significance. Zonal means are excluded

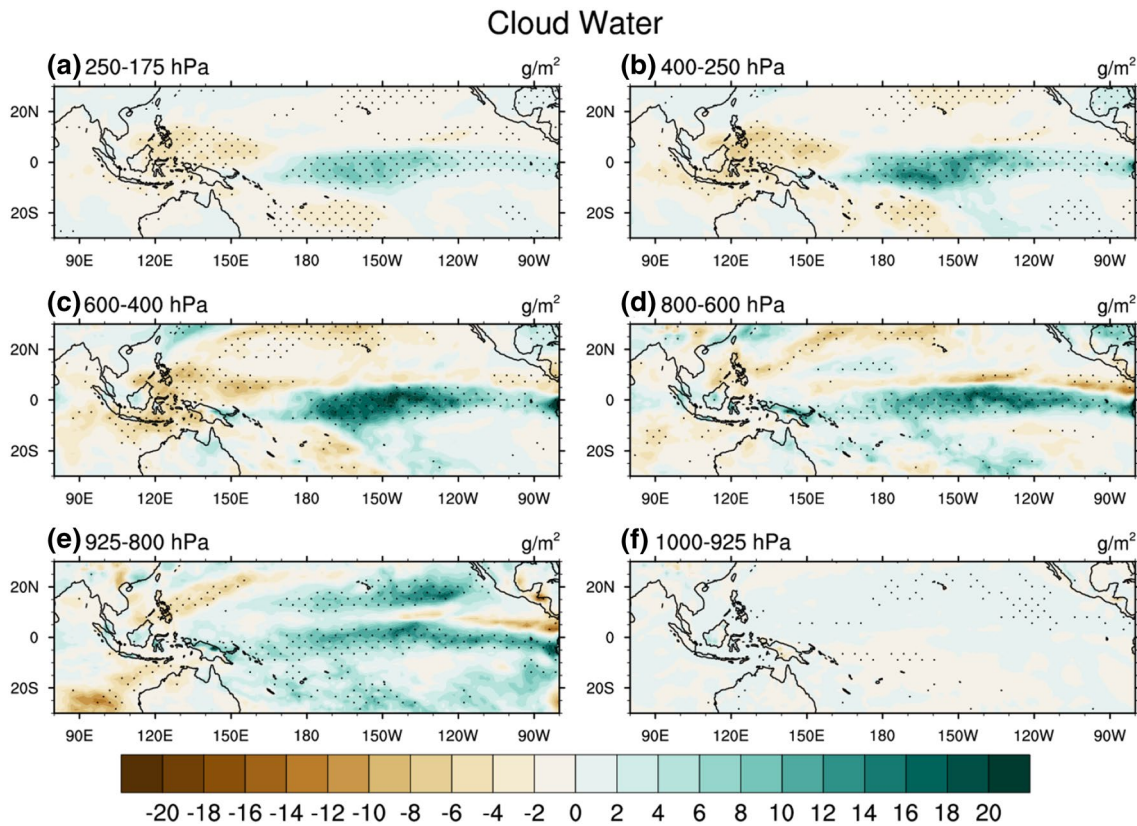


Fig. 5 As in Fig. 4 but for cloud water/ice content anomalies in units of g/m^2

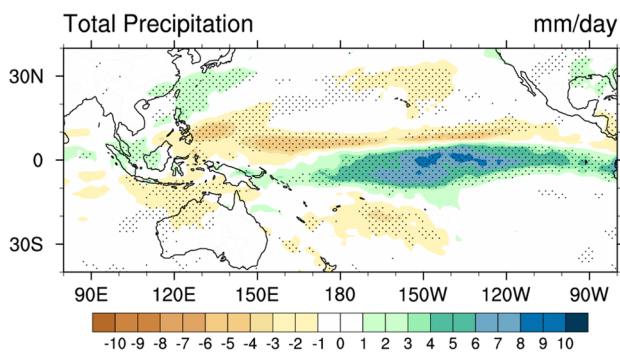


Fig. 6 Composite DJF-mean anomalies in El Niño winters of total precipitation in units of mm/day . Stippling indicates the 90% confidence level of statistical significance

pattern of cloud water/ice content anomalies in the middle and upper troposphere resembles greatly to that of the rainfall anomalies of the composite El Niño (Fig. 6), suggesting that most of condensation or latent heating anomaly takes place in the middle and upper troposphere. This conjecture is consistent with the vertical motion anomalies of the composite El Niño (Fig. 7). Specifically, the spatial patterns of vertical motion anomalies at 700, 500, and

300 hPa (Fig. 7b–d) are all similar to not only one another but also the cloud water/ice content anomalies at these layers (Fig. 5b–d) and rainfall anomalies (Fig. 6). The nearly perfect positive correlation among these spatial patterns indicates that the most latent heating anomalies take place in the layers between 700 and 300 hPa where both vertical motion and cloud content anomalies are strongest and their spatial patterns match the spatial pattern of rainfall anomalies. The pattern of downward motion anomalies with less clouds and reduction of rainfall over the western equatorial Pacific and upward motion anomalies with more clouds and enhancement of rainfall over the central-eastern Pacific is indicative of the weakening of the Walker Circulation during the mature phase of El Niño (Philander 1990, Hsu 1994; Power and Smith 2007). The dominance of the downward motion anomalies away from the equator, together with the dominance of the rising motion anomalies along the equatorial Pacific, is suggestive of the strengthening of the Hadley Circulation (Oort and Yienger 1996; Sun et al. 2013; Nguyen et al. 2013).

In summary, the key features of the non-air temperature changes over the tropical Pacific associated with the SST anomalies during El Niño winters include the following: (1) strengthening (weakening) of the upward thermal radiative

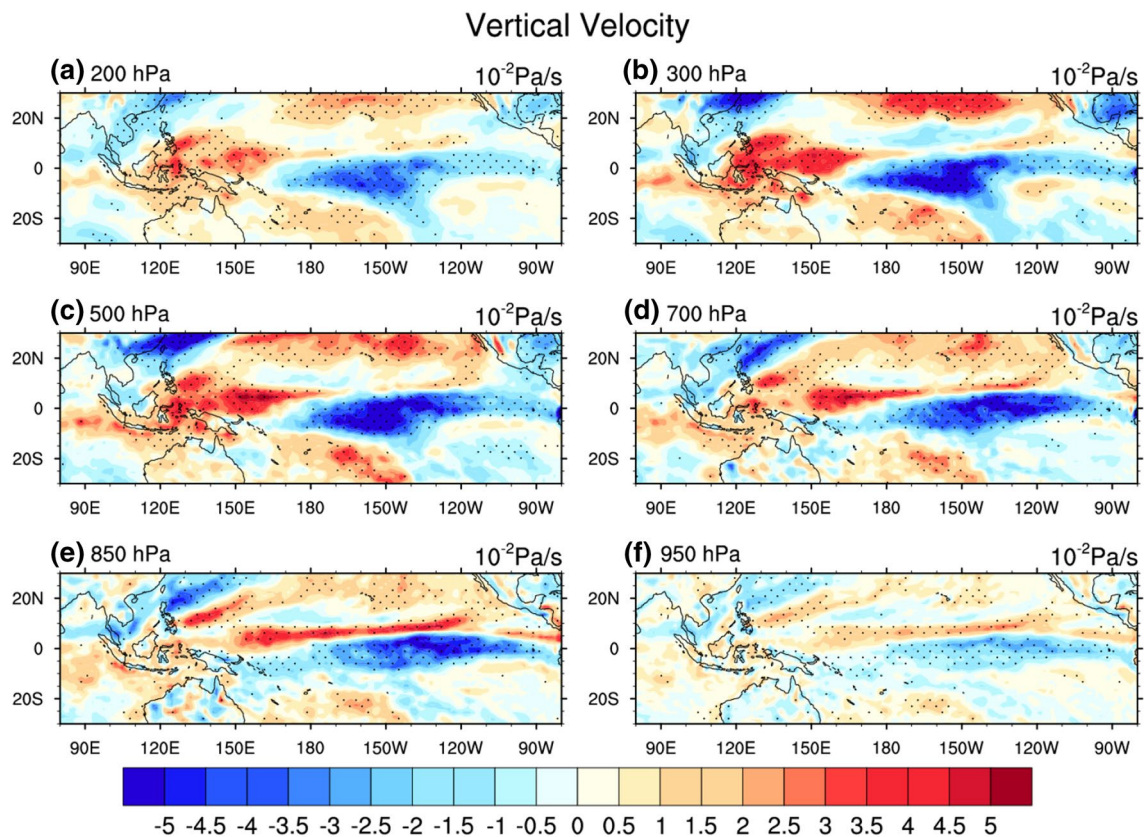


Fig. 7 As in Fig. 1 but for vertical velocity (ω) anomalies in units of Pa/s

fluxes emitted from the ocean surface in the central-eastern (western) equatorial Pacific, (2) moistening (drying) in the lower troposphere along the central-eastern (western) equatorial Pacific, and (3) more (less) latent heating release accompanied with more (less) clouds in the middle and upper troposphere along the central-eastern (western) equatorial Pacific. In the next section, we will consider the effects of radiative heating and non-radiative energy flux anomalies and examine how they are balanced by radiative thermal cooling anomalies associated with air temperature response.

5 Attribution of air temperature response to anomalies of radiative and non-radiative processes

The anomalies of the radiative thermal cooling rate associated with the air temperature anomalies at the six layers of 950, 850, 700, 500, 300, and 200 hPa (Fig. 8) exhibit similar spatial patterns as the air temperature anomalies shown in Fig. 3, because warm (cold) air temperature anomalies would emit more (less) thermal energy. We now attribute the air temperature anomalies to radiative and non-radiative

heating rate perturbations by examining their balance with the air temperature induced radiative cooling anomalies during El Niño winters. Figure 9 shows the PAP coefficients of each term on the RHS of (4) onto the left hand side (i.e., $\Delta^{(T)}R_j$ shown in Fig. 8) as a function of height.

It is seen from Fig. 9 that the radiative response (the orange and purple portions in 1000–925 hPa) to SST anomalies accounts for a large portion of the spatial pattern of radiative thermal cooling rate anomalies in the boundary layer (1000–925 hPa, $\Delta^{(T_1)}R_1$). A large portion of the energy emitted from the surface due to SST anomalies (Fig. 2b) is absorbed in the boundary layer (Fig. 10f), explaining why the air temperature response in the boundary layer resembles the SST anomalies greatly. The changes in upward thermal radiative fluxes related to the temperature anomalies in the boundary layer and at surface also lead to changes in the absorption of the layer of 925–800 hPa (Fig. 10e). This in turn leads to changes in the thermal cooling rate at this layer ($\Delta^{(T_2)}R_2$, Fig. 8e) and then changes in the boundary layer absorption of thermal emission from the layers above ($\Delta^{(T_{above})}Q_1$, Fig. 11f). The sum of the changes in the boundary absorption of thermal emission from other layers accounts for nearly 85% the spatial pattern of radiative thermal cooling rate anomalies in the

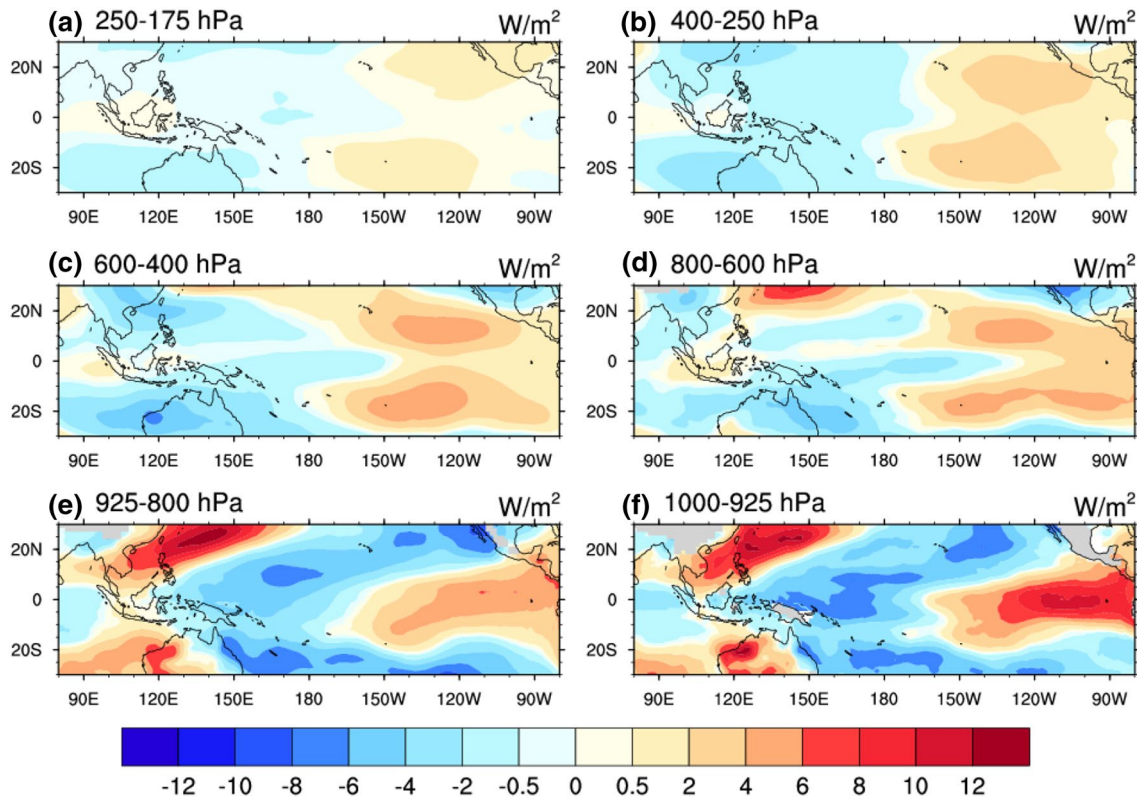


Fig. 8 Air temperature-induced radiative cooling rate anomalies in units of W/m^2 in the layers of **a** 250–150 hPa, **b** 400–250 hPa, **c** 600–400 hPa, **d** 800–600 hPa, **e** 925–800 hPa, and **f** 1000–925 hPa

boundary layer. In this case, the anomalous warming over the equatorial central and eastern Pacific but horseshoe-shape cooling over the western Pacific (Fig. 3f or Fig. 8f) can be explained nearly entirely by the boundary layer’s

absorption of anomalous longwave emission from ocean surface below.

In the tropics, positive (negative) surface pressure anomalies tend to collocate with negative (warm) temperature anomalies at the surface and in the lower troposphere. Therefore, the largely east–west see-saw pattern with a weak off-equator maximum centers in surface pressure anomalies (Fig. 2c) and in geopotential height anomalies in the boundary layer (Fig. 1e, f) are response to the thermal radiative heating anomalies associated with SST anomalies rather than the diabatic heating anomalies associated with convection. In particular, those off-equator anomalies shown in Fig. 1e, f or Fig. 3e, f are largely not part of the Gill-type response. Above the lower troposphere, the direct effect of SST anomalies diminishes very quickly (Fig. 10a–c). Because SST anomalies no longer play a direct role in causing air temperature change far above the boundary layer, the spatial pattern of air temperature anomalies differs from the SST anomaly pattern more and more as elevation goes up (see the orange and purple portions of the bars in Fig. 9).

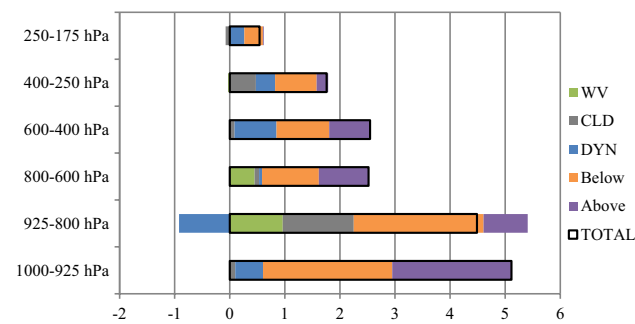


Fig. 9 Vertical profile of PAP coefficients of the patterns in Figs. 10, 11, 12, 13 and 14 onto the pattern shown in Fig. 8 (units W/m^2). Note that “Total” corresponds to $\sqrt{A^{-1} \int_A a^2(\Delta^{(T)}R_j)^2 \cos \phi d\lambda d\phi}$, the amplitude of $\Delta^{(T)}R_j$ at the j th layer over domain A ($90^\circ E-90^\circ W$ and $30^\circ S-30^\circ N$). It has been confirmed that the sum of the values represented by the color bars is approximately equal to the “Total” in every layer, indicating the approximation (3) is indeed valid

Displayed in Fig. 12 are the radiative heating rate anomalies due to the change in atmospheric water vapor ($\Delta^{(WV)}Q_j$). As discussed in Sejas et al. (2016), an increase

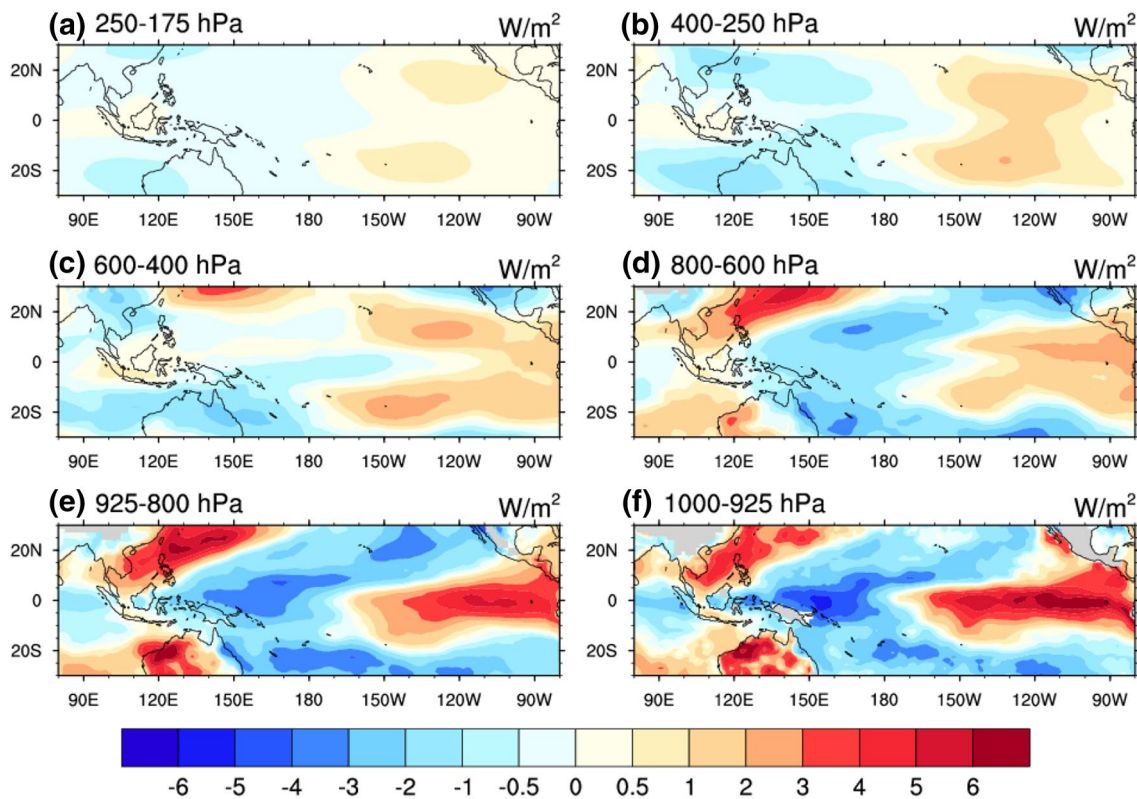


Fig. 10 As in Fig. 8 but for the absorption of anomalous longwave radiative fluxes (W/m^2) emitted from the layers below due to air/surface temperature anomalies there

of atmospheric greenhouse gases in a tropospheric layer, such as atmospheric water vapor, would lead to positive (negative) radiative heating anomalies in the layers below (above). The reversal can be said for a decrease of atmospheric water vapor in a tropospheric layer. Recall that atmospheric water anomalies (Fig. 4) tend to concentrate below the middle troposphere and are positively correlated with SST anomalies. This feature explains why the spatial pattern of $\Delta^{(WV)}Q_j$ in the lower troposphere (panels d–f of Fig. 12) is positively correlated with SST anomalies but negatively correlated with $\Delta^{(WV)}Q_j$ in the upper troposphere (panels a–c of Fig. 12). As a result, $\Delta^{(WV)}Q_j$ contributes to the air temperature changes positively and strongly in the lower troposphere but negatively and weakly in the upper troposphere (see the green portion of the bars in Fig. 9).

We have confirmed that different from the surface, throughout the atmosphere the longwave portion of the radiative heating rate anomalies ($\Delta^{(C)}Q_j$) or the greenhouse effect is greater than the shortwave portion or the reflection effect (Bergman and Hendon 2000; Wang and Su 2013). Therefore, the behavior of the net effect of $\Delta^{(C)}Q_j$ is similar to the effect of $\Delta^{(WV)}Q_j$, as far as the sign is concerned, namely large positive (weak negative) radiative heating anomalies below (above) the layer where cloud content anomalies are positive. Unlike atmospheric water vapor,

which mainly resides in the lower troposphere, clouds and their changes can take place largely in the upper troposphere. This is especially true for the equatorial region where cloud anomalies are associated with the changes in deep convection as both cloud and upward motion anomalies are large and are positively correlated one another even in the upper troposphere (Fig. 5 versus Fig. 7). In light of the aforementioned factors, one would expect positive values of $\Delta^{(C)}Q_j$ over the equatorial eastern and central Pacific throughout the troposphere but negative values over the western equatorial Pacific (Fig. 13) due to the weakening of the Walker Circulation or the weakening (strengthening) of deep convections over the western (central-eastern) equatorial Pacific. As a result, $\Delta^{(C)}Q_j$ contributes positively to the air temperature changes in the equatorial eastern and central Pacific throughout the troposphere. In the lower troposphere, $\Delta^{(C)}Q_j$ also contributes positively to the air temperature anomalies outside the equatorial basin, becoming the second leading contributor to $\Delta^{(T)}R_j$ over the entire tropical Pacific in the layer of 925–800 hPa (gray portion of the bars in Fig. 9). In the upper troposphere, $\Delta^{(C)}Q_j$ is weakly correlated with $\Delta^{(T)}R_j$ outside the equatorial Pacific basin, partially because the amplitude of cloud anomalies becomes weaker away from the equatorial latitude band in the upper troposphere. As a result, the positive contribution

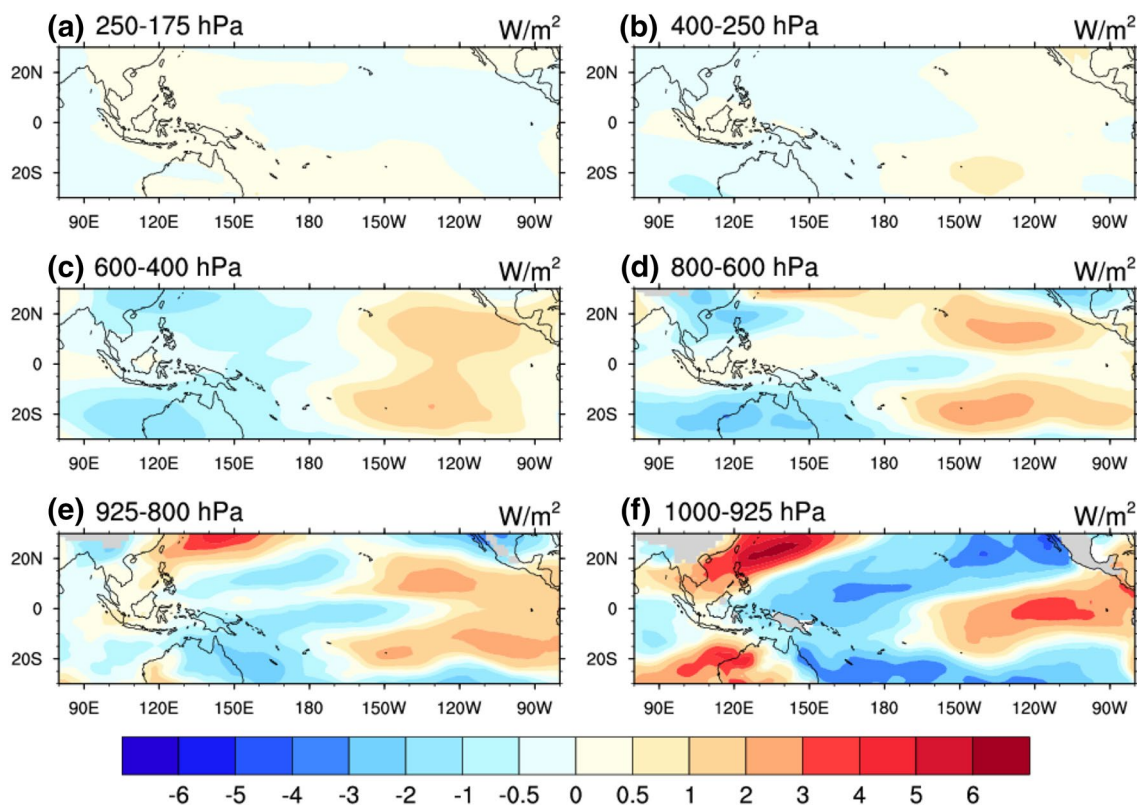


Fig. 11 As in Fig. 8 but for the absorption of anomalous longwave radiative fluxes (W/m^2) emitted from the layers above due to air temperature anomalies there

from $\Delta^{(C)}Q_j$ to $\Delta^{(T)}R_j$ becomes secondary in the upper troposphere.

The non-radiative heating anomalies ($\Delta^{(DYN)}Q_j$) include latent heat release anomalies and perturbations in energy redistributions by convective and large-scale atmospheric motions as well as changes in energy fluxes entering the atmosphere due to the changes in surface sensible and latent heat fluxes. Overall, the non-radiative heating anomalies are negatively correlated with the upward motion ($-\omega$) anomalies (i.e., Fig. 14 versus Fig. 7), particularly along the equatorial latitude band. This seems to indicate that the non-radiative heating anomalies are mainly associated with the energy redistributions by convective and large-scale atmospheric motions because latent heat release anomalies are expected to be positively correlated with upward motion anomalies. In other words, the negative (positive) values of $\Delta^{(DYN)}Q_j$ in Fig. 14 are indicative of divergence (convergence) of energy transport by convection and/or large-scale dynamics. The longitudinal pattern of $\Delta^{(DYN)}Q_j$ along the equatorial Pacific basin suggests an enhancement (reduction) of upward energy transport associated with the convection in the central (western) Pacific and

reduction of energy transport from the western equatorial Pacific to the central and eastern Pacific. Each of these two possible scenarios is a direct evidence of the weakening of the Walker Circulation during El Niño. The meridional pattern of $\Delta^{(DYN)}Q_j$ is indicative of strengthening (weakening) of poleward energy transport over the central-eastern (western) tropical Pacific sector. Overall, $\Delta^{(DYN)}Q_j$ contributes to air temperature changes positively in the middle and upper troposphere but negatively in the lower troposphere (the blue portion of the bars in Fig. 9). In particular, $\Delta^{(DYN)}Q_j$ becomes the leading contributor to $\Delta^{(T)}R_j$ at 200 hPa.

6 Conclusions

Using the ERA-Interim reanalysis data set, four major canonical El Niño events and eight neutral cases are selected for the period of 1979–2013. The DJF-mean differences between the two groups are regarded as the composite anomalies for the mature phase of the canonical El Niño. We have confirmed that the spatial pattern of air temperature anomalies in the lower troposphere is similar to

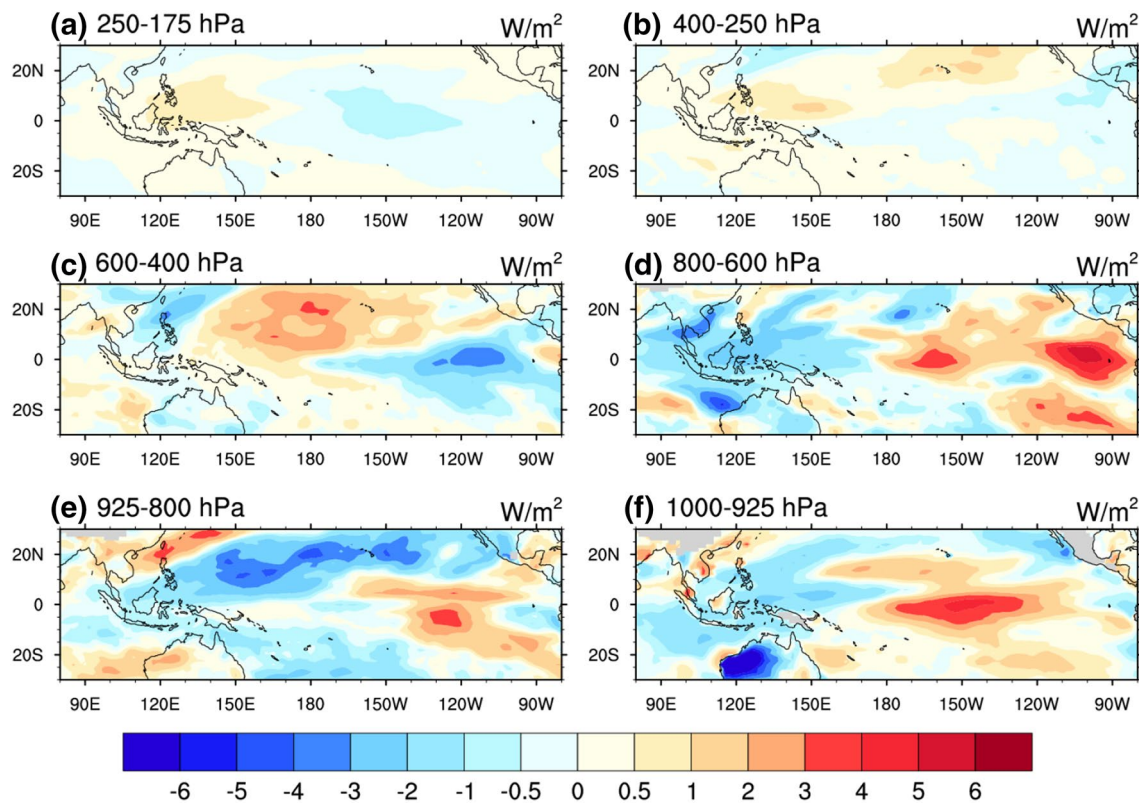


Fig. 12 As in Fig. 8 but for the water vapor-induced radiative heating rate anomalies in units of W/m^2

SST anomaly pattern and the Gill-type response begins to emerge mainly in the layers above 500 hPa with the maximum intensity at 300 hPa. To gain a better understanding of why the Gill-type response to SST anomalies over the tropical Pacific during El Niño mature phase is observed mainly in the upper troposphere, we examine the balance of thermal radiative cooling anomalies associated with air temperature response to SST anomalies with radiative transfer and dynamic processes. We have verified that analysis on these four major El Niño events individually yields more or less the same results as the composite El Niño. Therefore, our attribution analysis is robust.

Most of the anomalous upward longwave radiative fluxes associated SST anomalies are absorbed in the boundary layer. In response to such heating anomalies, air temperature anomalies in the boundary layer exhibit a similar spatial pattern as the SST anomalies so the associated thermal radiative cooling anomalies would balance out most of the absorbed energy. The moistening and more clouds in the lower troposphere produce positive radiative heating anomalies in the equatorial central and eastern Pacific but drying and less clouds in the western equatorial Pacific introduce negative radiative heating anomalies. The air temperature anomalies in the lower troposphere are

mainly in response to water vapor and cloud-induced radiative heating anomalies to reach a radiative equilibrium balance. The remaining part of the radiative heating anomalies is taken away by an enhancement (a reduction) of upward energy transport in the central-eastern (western) Pacific basin. The non-radiative heating anomalies associated with the changes in dynamics contribute secondarily to the air temperature anomalies in the lower troposphere. The dominance of the radiative heating anomalies associated with SST anomalies in the lower troposphere explains why the Gill-type response in the low levels is identifiable mainly in a dynamic model that does not include radiative heating processes.

Above the middle troposphere, the radiative effect due to water vapor feedback is weak. Thermal radiative cooling anomalies are mainly in balance with the sum of latent heating anomalies, the vertical and horizontal energy transport anomalies associated with atmospheric dynamic response, and the radiative heating anomalies due to cloud changes. The pattern of Gill-type response is attributed mainly to non-radiative heating anomalies associated with convective and large-scale energy transport. The radiative heating anomalies associated with the anomalies of high clouds also contribute positively to the Gill-type response.

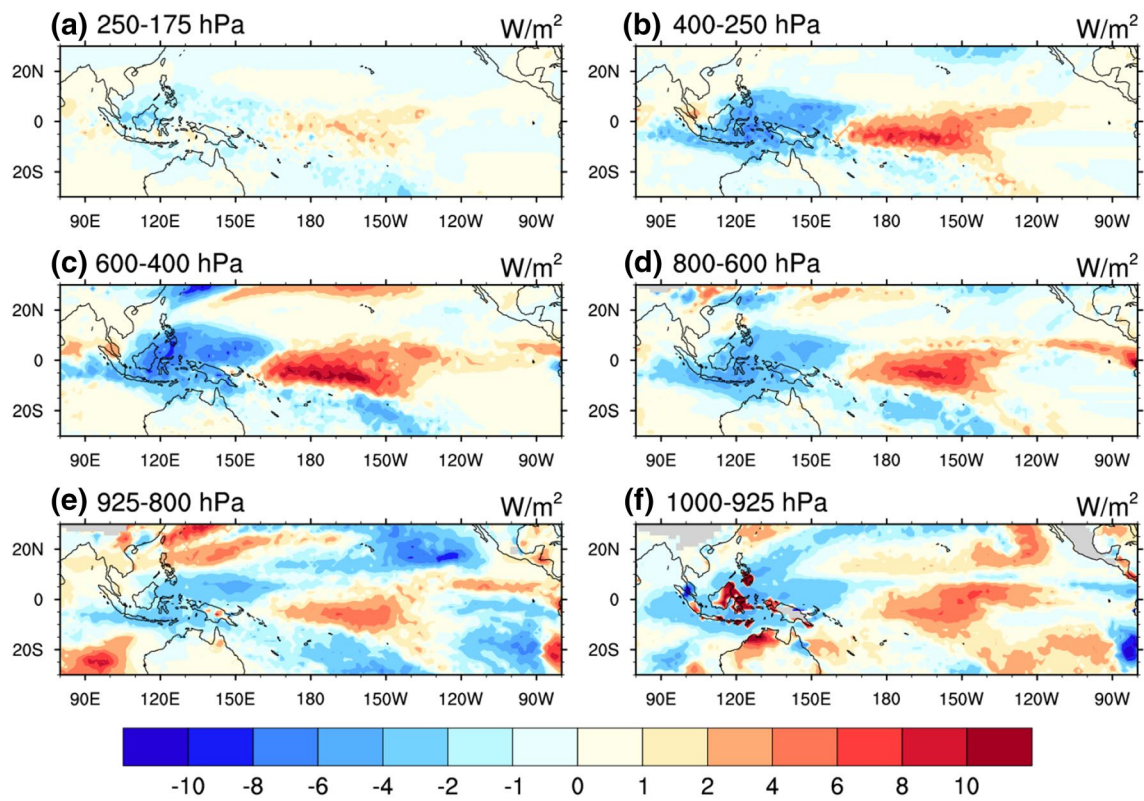


Fig. 13 As in Fig. 8 but for the cloud-induced radiative heating rate anomalies in units of W/m^2

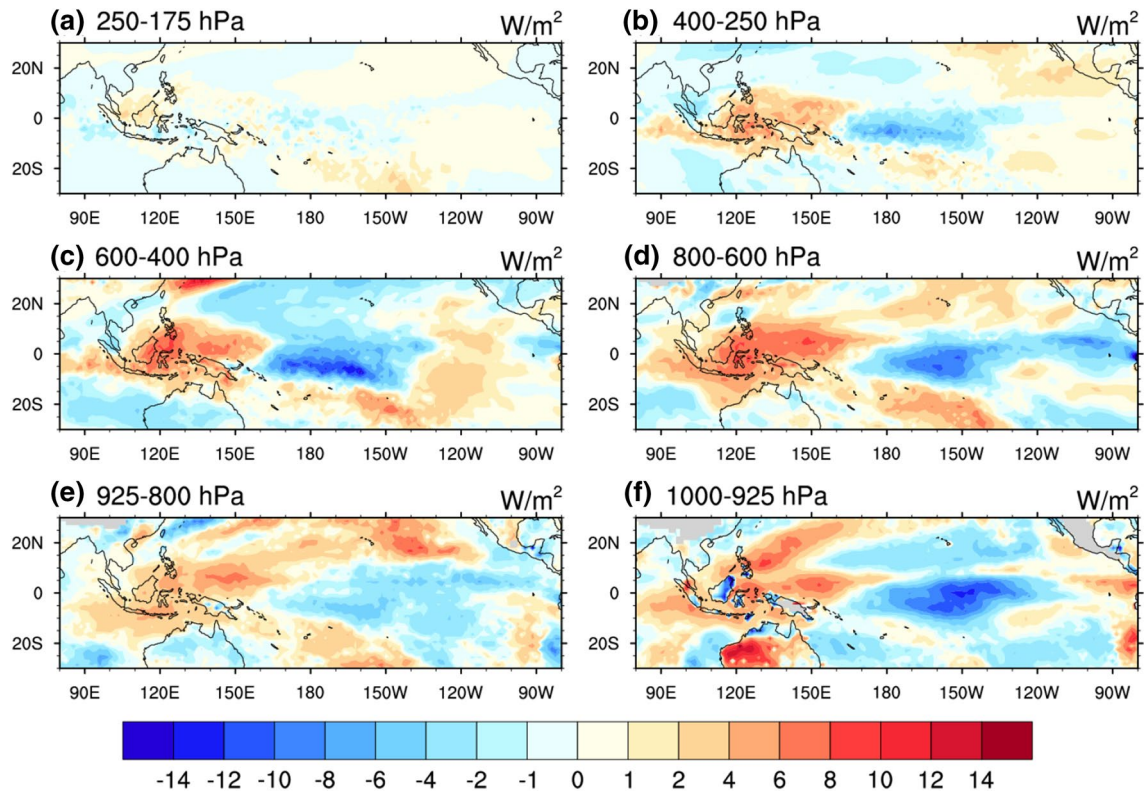


Fig. 14 As in Fig. 8 but for the non-radiative dynamic heating rate anomalies in units of W/m^2

This feature sheds light on why the Gill-type atmospheric response can be easily identifiable in the upper atmosphere.

Acknowledgements We appreciate the constructive comments from the two anonymous reviewers. This study was supported by The National Key Research and Development Program of China (2016YFA0602703), the National Key Research Program of China (2014CB953904), the National Natural Science Foundation of China (Grants 41661144019 and 41375081), the Jiangsu Collaborative Innovation Center for Climate Change and the CMA Guangzhou Joint Research Center for Atmospheric Sciences, China. MC is supported by grants from the National Science Foundation (AGS-1354834) and NASA Interdisciplinary Studies Program grant (NNH12ZDA001N-IDS). Calculations for this study were supported by the High-Performance Grid Computing Platform of the Sun Yat-sen University and the China National Supercomputer Center in Guangzhou. The data sets used in this study are all freely available on the official websites of <http://apps.ecmwf.int/datasets/data/interim-full-mnth/>.

Open Access This article is distributed under the terms of the Creative Commons Attribution 4.0 International License (<http://creativecommons.org/licenses/by/4.0/>), which permits unrestricted use, distribution, and reproduction in any medium, provided you give appropriate credit to the original author(s) and the source, provide a link to the Creative Commons license, and indicate if changes were made.

References

- Alexander MA, Bladé I, Newman M et al (2002) The atmospheric bridge: the influence of ENSO teleconnections on air–sea interaction over the global oceans. *J Climate* 15:2205–2231. doi:[10.1175/1520-0442\(2002\)015<2205:TABTIO>2.0.CO;2](https://doi.org/10.1175/1520-0442(2002)015<2205:TABTIO>2.0.CO;2)
- Ashok K, Behera SK, Rao SA et al (2007) El Niño Modoki and its possible teleconnection. *J Geophys Res Ocean*. doi:[10.1029/2006JC003798](https://doi.org/10.1029/2006JC003798)
- Back LE, Bretherton CS (2009) On the relationship between SST gradients, boundary layer winds, and convergence over the tropical oceans. *J Climate* 22:4182–4196. doi:[10.1175/2009JCLI2392.1](https://doi.org/10.1175/2009JCLI2392.1)
- Battisti DS, Sarachik ES, Hirst AC (1999) A consistent model for the large-scale steady surface atmospheric circulation in the tropics. *J Climate* 12:2956–2964. doi:[10.1175/1520-0442\(1999\)012<2956:ACMFTL>2.0.CO;2](https://doi.org/10.1175/1520-0442(1999)012<2956:ACMFTL>2.0.CO;2)
- Bergman JW, Hendon HH (2000) Cloud radiative forcing of the low-latitude tropospheric circulation: linear calculations. *J Atmos Sci* 57:2225–2245. doi:[10.1175/1520-0469\(2000\)057<2225:CRFOTL>2.0.CO;2](https://doi.org/10.1175/1520-0469(2000)057<2225:CRFOTL>2.0.CO;2)
- Bjerknes J (1969) Atmospheric teleconnections from the equatorial Pacific. *Mon Weather Rev* 97:163–172. doi:[10.1175/1520-0493\(1969\)097<0163:ATFTEP>2.3.CO;2](https://doi.org/10.1175/1520-0493(1969)097<0163:ATFTEP>2.3.CO;2)
- Chiang JCH, Zebiak SE, Cane M a (2001) Relative roles of elevated heating and surface temperature gradients in driving anomalous surface winds over tropical oceans. *J Atmos Sci* 58:1371–1394. doi:[10.1175/1520-0469\(2001\)058<1371:RROEHA>2.0.CO;2](https://doi.org/10.1175/1520-0469(2001)058<1371:RROEHA>2.0.CO;2)
- Dee DP, Uppala S (2009) Variational bias correction of satellite radiance data in the ERA-Interim reanalysis. *Q J R Meteorol Soc* 135:1830–1841. doi:[10.1002/qj.493](https://doi.org/10.1002/qj.493)
- Dee DP, Uppala SM, Simmons AJ et al (2011) The ERA-Interim reanalysis: configuration and performance of the data assimilation system. *Q J R Meteorol Soc* 137:553–597. doi:[10.1002/qj.828](https://doi.org/10.1002/qj.828)
- Deng Y, Park T-W, Cai M (2012) Process-based decomposition of the global surface temperature response to El Niño in boreal winter. *J Atmos Sci* 69:1706–1712. doi:[10.1175/JAS-D-12-023.1](https://doi.org/10.1175/JAS-D-12-023.1)
- DeWeaver E, Nigam S (2004) On the forcing of ENSO teleconnections by anomalous heating and cooling. *J Climate* 17:3225–3235. doi:[10.1175/1520-0442\(2004\)017<3225:OTFOET>2.0.CO;2](https://doi.org/10.1175/1520-0442(2004)017<3225:OTFOET>2.0.CO;2)
- Fu Q, Liou KN (1992) On the correlated k-distribution method for radiative transfer in nonhomogeneous atmospheres. *J Atmos Sci* 49:2139–2156
- Fu Q, Liou KN (1993) Parameterization of the radiative properties of cirrus clouds. *J Atmos Sci* 50:2008–2025
- Gill AE (1980) Some simple solutions for heat induced tropical circulation. *Q J R Meteorol Soc* 106:447–462
- Hoskins BJ, Karoly DJ (1981) The steady linear response of a spherical atmosphere to thermal and orographic forcing. *J Atmos Sci* 38:1179–1196
- Hsu HH (1994) Relationship between tropical heating and global circulation—interannual variability. *J Geophys Res* 99:10473–10489
- Hu X, Yang S, Cai M (2016) Contrasting the eastern Pacific El Niño and the central Pacific El Niño: process-based feedback attribution. *Climate Dyn* 47:2413–2424. doi:[10.1007/s00382-015-2971-9](https://doi.org/10.1007/s00382-015-2971-9)
- Kao HY, Yu JY (2009) Contrasting eastern-Pacific and central-Pacific types of ENSO. *J Climate* 22:615–632. doi:[10.1175/2008JCLI2309.1](https://doi.org/10.1175/2008JCLI2309.1)
- Larkin NK (2005) Global seasonal temperature and precipitation anomalies during El Niño autumn and winter. *Geophys Res Lett* 32:L16705. doi:[10.1029/2005GL022860](https://doi.org/10.1029/2005GL022860)
- Lee SK, Wang C, Mapes BE (2009) A simple atmospheric model of the local and teleconnection responses to tropical heating anomalies. *J Climate* 22:272–284. doi:[10.1175/2008JCLI2303.1](https://doi.org/10.1175/2008JCLI2303.1)
- Lindzen RS, Nigam S (1987) On the role of sea surface temperature gradients in forcing low-level winds and convergence in the Tropics. *J Atmos Sci* 44:2418–2436. doi:[10.1175/1520-0469\(1987\)044<2418:OTROSS>2.0.CO;2](https://doi.org/10.1175/1520-0469(1987)044<2418:OTROSS>2.0.CO;2)
- Lyon B, Barnston AG (2005) ENSO and the spatial extent of interannual precipitation extremes in tropical land areas. *J Climate* 18:5095–5109. doi:[10.1175/JCLI3598.1](https://doi.org/10.1175/JCLI3598.1)
- Nguyen H, Evans A, Lucas C et al (2013) The Hadley circulation in reanalyses: climatology, variability, and change. *J Climate* 26:3357–3376. doi:[10.1175/JCLI-D-12-00224.1](https://doi.org/10.1175/JCLI-D-12-00224.1)
- Oort AH, Yienger JJ (1996) Observed interannual variability in the Hadley circulation and its connection to ENSO. *J Climate* 9:2751–2767
- Philander SG (1990) *El Niño, La Niña, and the southern oscillation*. Academic Press, Cambridge, 293
- Power SB, Smith IN (2007) Weakening of the Walker Circulation and apparent dominance of El Niño both reach record levels, but has ENSO really changed? *Geophys Res Lett* 34:L18702. doi:[10.1029/2007GL030854](https://doi.org/10.1029/2007GL030854)
- Prabhakara C, Short DA, Vollmer BE (1985) El Niño and atmospheric water vapor: observations from Nimbus 7 SMMR. *J Clim Appl Meteorol* 24:1311–1324
- Rasmusson EM, Carpenter TH (1982) Variations in tropical sea surface temperature and surface wind fields associated with the southern oscillation/El Niño. *Mon Weather Rev* 110:354–384
- Rasmusson EM, Kingse Mo (1993) Linkages between 200-mb tropical and extratropical circulation anomalies during the 1986–1989 ENSO cycle. *J Climate* 6:595–616
- Rasmusson EM, Wallace JM (1983) Meteorological aspects of the El Niño/southern oscillation. *Science* 222:1195–1202. doi:[10.1126/science.222.4629.1195](https://doi.org/10.1126/science.222.4629.1195)

- Scherllin-Pirscher B, Steiner AK, Kirchengast G et al (2011) Empirical analysis and modeling of errors of atmospheric profiles from GPS radio occultation. *Atmos Meas Tech* 4:1875–1890. doi:[10.5194/amt-4-1875-2011](https://doi.org/10.5194/amt-4-1875-2011)
- Sejas SA, Cai M, Liu G et al (2016) A Lagrangian view of longwave radiative fluxes for understanding the direct heating response to a CO₂ increase. *J Geophys Res Atmos* 121:6191–6214. doi:[10.1002/2015JD024738](https://doi.org/10.1002/2015JD024738)
- Sun Y, Zhou TJ, Zhang LX (2013) Observational analysis and numerical simulation of the interannual variability of the boreal winter Hadley circulation over the recent 30 years. *Sci China Earth Sci* 56:647–661. doi:[10.1007/s11430-012-4497-x](https://doi.org/10.1007/s11430-012-4497-x)
- Takahashi H, Su H, Jiang JH et al (2013) Tropical water vapor variations during the 2006–2007 and 2009–2010 El Niños: satellite observation and GFDL AM2.1 simulation. *J Geophys Res Atmos* 118:8910–8920. doi:[10.1002/jgrd.50684](https://doi.org/10.1002/jgrd.50684)
- Trenberth KE, Branstator GW, Karoly D et al (1998) Progress during TOGA in understanding and modeling global teleconnections associated with tropical sea surface temperatures. *J Geophys Res* 103:14291–14324. doi:[10.1029/97jc01444](https://doi.org/10.1029/97jc01444)
- Wang H, Su W (2013) Evaluating and understanding top of the atmosphere cloud radiative effects in Intergovernmental Panel on Climate Change (IPCC) Fifth Assessment Report (AR5) Coupled Model Intercomparison Project Phase 5 (CMIP5) models using satellite observations. *J Geophys Res Atmos* 118:683–699. doi:[10.1029/2012JD018619](https://doi.org/10.1029/2012JD018619)
- Wang B, Wu R, Fu X (2000) Pacific–East Asian teleconnection: how does ENSO affect East Asian climate? *J Climate* 13:1517–1536. doi:[10.1175/1520-0442\(2000\)013<1517:PEATHD>2.0.CO;2](https://doi.org/10.1175/1520-0442(2000)013<1517:PEATHD>2.0.CO;2)
- Wang H, Kumar A, Wang W, Xue Y (2012) Influence of ENSO on Pacific decadal variability: an analysis based on the NCEP climate forecast system. *J Climate* 25:6136–6151. doi:[10.1175/JCLI-D-11-00573.1](https://doi.org/10.1175/JCLI-D-11-00573.1)
- Wu Z (2003) A shallow CISK, deep equilibrium mechanism for the interaction between large-scale convection and large-scale circulations in the tropics. *J Atmos Sci* 60:377–392. doi:[10.1175/1520-0469\(2003\)060<0377:ASCDEM>2.0.CO;2](https://doi.org/10.1175/1520-0469(2003)060<0377:ASCDEM>2.0.CO;2)
- Wu Z, Sarachik ES, Battisti DS (2000) Vertical structure of convective heating and the three-dimensional structure of the forced circulation on an equatorial beta plane. *J Atmos Sci* 57:2169–2187. doi:[10.1175/1520-0469\(2000\)057<2169:VSOCHA>2.0.CO;2](https://doi.org/10.1175/1520-0469(2000)057<2169:VSOCHA>2.0.CO;2)
- Yuan Y, Yang S (2012) Impacts of different types of El Niño on the East Asian climate: focus on ENSO cycles. *J Climate* 25:7702–7722. doi:[10.1175/JCLI-D-11-00576.1](https://doi.org/10.1175/JCLI-D-11-00576.1)
- Zebiak SE (1986) Atmospheric convergence feedback in a simple model for El Niño. *Mon Weather Rev* 114:1263–1271
- Zhang X, Lin H, Jiang J (2012) Global response to tropical diabatic heating variability in boreal winter. *Adv Atmos Sci* 29:369–380. doi:[10.1007/s00376-011-1049-9](https://doi.org/10.1007/s00376-011-1049-9)